Published in final edited form as:
IEEE Trans Biomed Eng. 2012 July ; 59(7): 1902–1911. doi:10.1109/TBME.2012.2192118.

Biopsy Needle Artifact Localization in MRI-guided Robotic Transrectal Prostate Intervention

Sang-Eun Song [Member, IEEE],
Laboratory for Computational Sensing and Robotics, Johns Hopkins University, Baltimore, Maryland, USA, and is presently with Surgical Navigation and Robotics Laboratory, Brigham and Women's Hospital, Harvard Medical School, Boston, Massachusetts, USA

Nathan B. Cho,
Laboratory for Computational Sensing and Robotics and the Department of Mechanical Engineering, Johns Hopkins University, Baltimore, Maryland, USA

Iulian Iordachita [Member IEEE],
Laboratory for Computational Sensing and Robotics and the Department of Mechanical Engineering, Johns Hopkins University, Baltimore, Maryland, USA

Peter Guion [Member, IEEE],
Radiation Oncology Branch, National Cancer Institute, National Institutes of Health, Bethesda, Maryland, USA

Gabor Fichtinger [Member, IEEE],
School of Computing, Queen's University, Kingston, Ontario, Canada

Aradhana Kaushal, M.D.,
Radiation Oncology Branch, National Cancer Institute, National Institutes of Health, Bethesda, Maryland, USA

Kevin Camphausen, M.D., and
Radiation Oncology Branch, National Cancer Institute, National Institutes of Health, Bethesda, Maryland, USA

Louis L. Whitcomb [Fellow, IEEE]
Laboratory for Computational Sensing and Robotics and the Department of Mechanical Engineering, Johns Hopkins University, Baltimore, Maryland, USA

Abstract

Recently a number of robotic intervention systems for magnetic resonance image (MRI) guided needle placement in the prostate have been reported. In MRI-guided needle interventions, after a needle is inserted, the needle position is often confirmed with a volumetric MRI scan. Commonly used titanium needles are not directly visible in an MR image, but they generate a susceptibility artifact in the immediate neighborhood of the needle. This paper reports the results of a quantitative study of the relationship between the true position of titanium biopsy needle and the corresponding needle artifact position in MR images, thereby providing a better understanding of the influence of needle artifact on targeting errors. The titanium needle tip artifact extended 9 mm beyond the actual needle tip location with tendency to bend towards the scanner's B_0 magnetic

field direction, and axially displaced 0.38 mm and 0.32 mm (mean) in scanner's frequency and phase encoding direction, respectively.

Index Terms

Needle artifact; prostate intervention; robotic intervention; transrectal biopsy

I. Introduction

Recently, several magnetic resonance image (MRI) guided robotic systems for prostate needle intervention have been reported. For example, the authors and collaborators reported several generations of MRI-guided robotic systems for trans-rectal prostate intervention and clinically that has been employed in clinical procedures [2–7]. In clinical procedures with these systems, the clinician confirms the inserted needle position from a series of MR images. The MRI scanner cannot directly image the metal needle, however. The MR image shows a loss of signal near the needle location due to a susceptibility artifact induced by the needle itself - often termed a "needle artifact." The objective of this study is to experimentally evaluate the spatial relationship between the location of the needle artifact in the MR image and the true needle position. A systematic empirical understanding of the needle artifact displacement will enable more accurate analysis of needle targeting accuracy in MRI-guided needle intervention procedures in the prostate.

II. Background

A. Prostate Cancer and Core Biopsy

Prostate cancer is the most common cancer in men in the United States. In 2012, an estimated 241,740 men will be diagnosed with prostate cancer and an estimated 28,170 will die of this disease [8].

The "Gold Standard" of guiding biopsy, as well as of most local therapies, is transrectal ultrasound (TRUS) [9]. The physician manually places a TRUS probe in the rectum of the patient and, under ultrasound guidance, inserts a biopsy needle through the wall of the rectum into the prostate gland. The needle removes a tissue sample, which is examined by pathologists to determine if cancer is present. Several biopsy samples are taken from different areas of the prostate. Usually six to eighteen cores are removed from upper, mid, and lower areas of the left and right sides to obtain a representative sample of the gland and determine the degree and extent of cancer. Each year approximately 1.5 million prostate biopsy procedures are performed.

TRUS-guided prostate biopsy is widely employed due to its real-time nature, relative low cost, and ease of use. Numerous studies have shown that TRUS-guided prostate biopsy fails to detect cancer in at least 20% of patients with cancer [10–13]. Other studies report that TRUS biopsies are limited by low sensitivity of 60% with only 25% positive predictive value [14]. TRUS imaging is generally unable to differentiate between healthy tissue and lesions in the prostate.

B. MRI-guided Robotic Intervention

MRI possesses many of the capabilities that TRUS is lacking. MRI is an attractive choice for image guidance, primarily due to its high sensitivity for detecting prostate tumors [15], high spatial resolution, excellent soft tissue contrast, multi-planar volumetric imaging capabilities, and ability to support focal therapies [16]. Several different systems for MRI-guided needle access of the prostate have been reported. They include the following:

1. Transrectal Approach: In [2–7] the authors and collaborators reported the development and clinical evaluation of a MRI-guided system for transrectal prostate biopsy, therapy injection, and marker placement. The system, called the APT (Access to Prostate Tissue), contains a single-loop MRI endorectal imaging coil and employs active or passive tracking for device localization. In vivo and in vitro accuracy results were reported. This clinical prototype has been successfully used in over 50 patient procedures to date. Beyersdorff [17] and Engelhard [18] reported MRI-guided transrectal needle biopsies in clinical studies with a system (Invivo Germany GmbH, Schwerin, Germany) employing manual alignment of a needle sleeve. In [19] Schouten reported a MRI-compatible pneumatically actuated transrectal robot. Elhawary reported a prototype robotic system using linear piezo-ceramic motors for transrectal prostate biopsy [20]. Recently, Yakar reported a pneumatically actuated MRI compatible robot for prostate biopsy guidance [21].
2. Transperineal Approach: MRI-guided transperineal prostate intervention has been demonstrated in clinical studies inside in open MRI scanners [22] and in conventional closed MRI scanners [3]. The surgical assistant robot reported by Chinzei [23] was adapted to assist transperineal intra-prostatic needle placement [24]. Tadakuma reported the use of dielectric elastomer actuators in a pre-clinical prototype robot for transperineal needle placement in the prostate [25]. Stoianovici reported pre-clinical phantom experiments with a pneumatic system for transperineal brachytherapy [26]. In [27–29] the authors and collaborators reported phantom experiments with a device with a pneumatically actuated needle guide and manual needle insertion for transperineal needle placement in the prostate. Goldenberg reported phantom targeting and MRI compatibility tests for a robotic system employing ultrasonic actuators for closed MRI scanners [30]. In [31], van den Bosch reported a hydraulically and pneumatically actuated tapping robot. Recently, Su reported a real-time MRI-guided needle placement robot with fiber optic force sensing [32].
3. Transgluteal Approach: Zangos reported preliminary clinical results with 25 patients using the transgluteal approach with an open configuration 0.2T MRI scanner [33], with targeting based on prior diagnostic images acquired with higher field strength MRI. In [34] Zangos reported usage of the Innomotion pneumatic robot in a cadaver study at 1.5T for transgluteal prostate needle placements. Recently, a patient study of the robotic intervention was reported in [35, 36].

C. MRI-guided Transrectal Needle Targeting Accuracy

In MRI-guided needle procedures, a confirmation image of the needle location is acquired after the needle is inserted so that confirms the accuracy of MRI-guided needle targeting and so that the clinician can evaluate the needle placement accuracy. Titanium biopsy needles, which are the most commonly used in prostate biopsy, are not directly visible in MRI, but they generate a susceptibility artifact in the MR image in the neighborhood of the titanium needle. This artifact is commonly termed as “needle void” or “needle artifact.” The needle artifact, which is seen by clinician to confirm biopsy targeting accuracy, is typically displaced from the true needle position, and differs in size and shape from the needle itself.

D. Previously Reported Needle Artifact Studies

Many previous studies have addressed needle artifact versus true needle position, with a variety of needles, scanning sequences, and orientations with respect to B_0, frequency encoding direction, gradient encoding direction.

Blumenfeld [37] reported that needle placement error is mainly due to needle deflection especially with asymmetrically beveled needles. Lufkin [38] described needle artifact in a MRI-guided needle placement that selectively rotates scan plane. Lewin [39] reported a needle artifact study to evaluate MR imaging accuracy at 0.2T and 1.5T with multiple sequences and needle rotations. They found that when the needle is perpendicular to the frequency encoding direction and the static magnetic field (B_0), the artifacts are much more apparent. DiMaio [24] conducted a needle artifact study in 3T MRI using a rotating needle holder with ex-vivo tissue samples, concluding that artifacts are shifted along the frequency encoding direction.

Wachowicz [40] modeled brachytherapy seed artifacts in various directions with respect to B_0 in order to create distortion maps, and compared these simulated images to actual imagery. The results indicated good agreement, suggesting that artifact patterns depend on the encoding directions and orientations of the B_0 field and seed. Lagerburg [41] studied artifacts of iodine seeds placed at the needle tip in MRI-guided prostate brachytherapy, reporting that determination of the exact seed position was difficult because of the large artifact at the tip of the needle. Thomas [42] also investigated the effects of artifact size on the ability to localize multiple seeds in close proximity.

Our study addresses the case of a 3T scanner, using needle confirmation scan sequences that limit the effective Specific Absorption Rate (SAR) to below the FDA guidelines of 8 W/kg for the torso [43], including the local effective increase in SAR due to the presence of the biopsy needle [6, 44].

III. Materials and Methods

A series of preliminary tests revealed that variation in titanium needle size (14G, 16G and 18G) had a negligible effect on the size and shape of the needle void, hence a widely used commercially available 14G MR-compatible biopsy needle was employed in the experiments reported herein. Commercially available prostate phantoms have limited target volume and their multiple layers may cause needle bending during insertion. To minimize physical needle deflection and concentrate solely on needle void artifact, a larger and uniformly soft custom-made gel phantom was constructed for the experiment.

A. Experimental Setup

Fig. 1 shows the needle artifact experiment setup using the APT robot [4], in a 3T Philips Achieva MRI scanner (Philips Medical Systems, Best, NL). A custom-made gel phantom (plant starch mixed with water and heated) was used as a soft tissue phantom. The phantom was placed on the scanner table between two liquid imaging phantoms. In order to identify the true needle position, a 14G sized glass rod with conical tip was used. For the needle artifact, a 150 mm 14G MRI-compatible automatic titanium biopsy gun (product number 11705, Invivo, Orlando, Florida, USA), which is widely used for patient procedures, was employed. The titanium needle has a bevel tip but the beveled direction was not considered in the experiment since the bevel angle is not actively controlled in the robotic procedures. An endorectal imaging coil embedded in the APT robot and a two-channel surface coil placed under the phantom were used to obtain T2-weight axial Turbo Spin Echo (TSE) images (Table 1) of the glass rod and titanium needle. This is identical to the setup used for the clinical cases in which the APT has been used.

After the robot and phantom were securely positioned, a series of registration scans were obtained to determine the location of four fiducial markers (Beekley Corp., Bristol, CT), embedded in the APT robot at predefined positions. 3D Slicer with ProstateNav module was used for registration. The ProstateNav software module is designed for APT robot

registration, targeting and evaluation, as reported in detail in [5]. However, in this experiment, only registration was performed. Fig. 2 shows a screenshot of 3D Slicer ProstateNav module.

B. Needle Positioning

To observe the needle artifact in various needle orientations, fifteen distinct needle orientations that cover APT's targeting range were selected. The orientations consist of five rotation angles (−30°, −15°, 0°, 15°, and 30°) and three tilt angles (18°, 28°, and 38°). In preliminary pilot studies, no noticeable artifact variation was observed with insertion depth variation, so an insertion depth of 140 mm was employed uniformly. The fifteen orientations were manually set in sequence. At each insertion orientation, a glass rod was first inserted and a confirmation image series was taken, then the 14G titanium biopsy needle was inserted and a second confirmation image series was similarly obtained. In total, 30 sets (five rotation angles and three tilt angles for each of the glass rod and titanium needle) of volumetric confirmation images were obtained.

Fig. 3 illustrates a CAD model of the needle insertion angles in the scanner's RAS coordinate frame. For 0° rotation angle, the angle between the needle axis to B_0 magnetic field direction angle is approximately 35°, 45°, and 55° for tilt angles of 18°, 28°, and 38°, respectively.

C. Needle Artifact Localization

The center of the needle artifact was selected manually in each of the image slices of all 30 volumetric scans. Fig. 4 shows a series of cropped images that represent typical artifact patterns of a glass rod and a titanium needle.

The manually selected needle-artifact center positions were then used to compute the least-square fit to a line in three-dimensional space. The titanium needle tip creates distinctive artifact that deviates from the needle body artifact in both size and direction. Hence, the titanium needle tip artifact, which appears to extend beyond the glass rod tip, was excluded from the least-square fitting.

IV. Results

Thirty volumetric MR transverse scans of needles were analyzed with the needles positioned in fifteen distinct needle positions, in order to identify the center of the needle image artifact in each of the axial image slices. For each of fifteen needle guide positions two scans were analyzed: one volumetric confirmation scan of the 14G titanium biopsy needle and one confirmation scan of the 14G glass rod, a total of 30 volumetric confirmation scans.

A. Needle Artifact Geometry

Fig. 5 shows representative sagittal and coronal views of the needle void locations observed on each transverse slice for the titanium needle and the glass rod and for their corresponding least-square best-fit lines. For the transverse image slices in which the needles were present, the centers of the voids for both the glass rod and titanium needle were found to be co-linear.

Table 2 reports the RMS residuals (mm) for the least-square line fits for each of the 15 insertion positions for the glass rod (Table 2, top) and the titanium needle (Table 2, bottom). This table shows that the RMS residuals for both the glass rod and the titanium needle are smaller than the pixel width of 0.86 mm. The typical value is under 0.1 mm, one order of

magnitude smaller than the pixel width. The maximum observed RMS residual was 0.17 mm.

B. Needle Artifact Localization

The needle artifact position errors in the transverse plane for the fifteen tested needle orientations are plotted in Fig. 6. The plotted points represent the transverse plane XY displacement (in mm) between the center of the titanium needle void and the actual needle position for all transverse image slices physically intersecting the needles. The actual glass and titanium needle locations are identical in each case, but their imaged locations differ. The actual needle position is given by the image of the glass rod, but the titanium needle image void position (i.e. the needle void) is displaced from the actual needle position. These data represent needle tilt angles of 18° 28° and 38° and needle rotation angles of −30°, −15°, 0°, +15°, and +30°.

Fig. 6 (a) shows boxplots of the titanium needle void displacement in the Y (anterior) frequency encoding direction for each of the 15 combinations of needle tilt angles and rotation angles. These data indicate that the needle void displacement in the frequency encoding direction varies significantly with the needle tilt (i.e. the angle to B_0) and is less sensitive to the needle rotation angle. The mean Y displacement for tilt angle of 18°, 28° and 38° over all rotation angles was, respectively, −0.49 mm, +0.39 mm, and +1.17 mm. The mean Y displacement increased slightly with increasing rotation angle. In summary:

1. At needle tilt angles of 18°, the mean Y displacement was small but varied from −0.74 mm to −0.30 mm, but with a large standard deviation of 0.84 mm to 0.99 mm.
2. At needle tilt angles of 28°, the mean Y displacement varied from −0.19 mm to +0.74 mm, with a standard deviation of 0.23 mm to 0.59 mm.
3. At needle tilt angles of 38°, the mean Y displacement varied from +0.96 mm to +1.44 mm, with a standard deviation of 0.31 mm to 0.59 mm.

Fig. 6 (b) shows boxplots of the titanium needle void displacement in the X (right) phase encoding direction for each of the 15 combinations of needle tilt angles and rotation angles. These data indicate the needle void displacement in the phase encoding direction varies little with variations in needle tilt (i.e. the angle to B_0) and needle rotation. The mean X displacement for tilt angle of 18°, 28° and 38° over all rotation angles was, respectively, +0.40 mm, +0.37 mm, and +0.24 mm. The needle displacements in the phase encoding direction have means of magnitude 0.5 mm or less, and very small standard deviations of 0.4 mm or less.

Fig. 6 (c) shows boxplots of the titanium needle void total displacement distance for each of the 15 combinations of needle tilt angles and rotation angles. The total displacement distance for tilt angle of 18°, 28° and 38° over all rotation angles was, respectively, +1.06 mm, +0.70 mm, and +1.23 mm.

Table 3 shows the transverse plane needle artifact position error mean and standard deviation averaged over the 15 tested needle orientations. The average displacement in the Y (anterior) frequency encoding direction is 0.38 mm with a comparative standard deviation of 0.56 mm. The average displacement in the X (right) phase encoding direction is 0.32 mm with a small standard deviation of 0.13 mm.

An alternative graph for the transverse plane needle artifact position errors is given in Fig. 7. The plots show the transverse plane difference between the center of the titanium needle void and the center of the glass needle void for all transverse image slices physically

intersecting the needles. The actual needle locations are physically identical in each case, but the titanium needle image void is displaced with respect to the actual needle position that is given by the glass rod. From the practical standpoint of targeting accuracy evaluation, this graph is a very useful tool for quick estimation (by interpolation in vertical and/or horizontal direction) of the errors for any combination needle angle – rotating angle.

C. Needle Tip Artifact

The needle void created by a titanium needle in MR images extends beyond the physical tip of the needle. In these images, the titanium needle void was present in three transverse slices (i.e. a total of 9 mm) beyond the physical tip of the needle itself. Moreover, this extension of the titanium needle artifact exhibited a pronounced curvature in the direction of the B_0 magnetic field. This pronounced effect is shown in Fig. 8 and Fig. 9.

Fig. 8 shows representative plots of the glass rod and the titanium needle artifact center positions and the fitted line at various insertion angles, including entire recognizable titanium needle artifact. The “bending” of the titanium needle tip artifact towards B_0 direction is highlighted within a circle.

In Fig. 9 the glass rod and needle contours are superimposed (based on fitted axis data) on the same sagittal plan containing the glass rod and the needle axes, respectively. The needle tip artifact is beyond the actual needle tip and is “bent” towards the B_0 direction. Also, the artifact around needle biopsy gap segment (where inner stylet has less material i.e. the space for tissue) is smaller than the rest.

V. Discussion

The goal of this study is to evaluate quantitatively the relationship between the true position of titanium biopsy needle and the corresponding needle artifact position in MR images. In a phantom study we found the MR image needle void to be displaced from the true needle position by up to about 1 mm (mean value, total displacement), and that the displacement varies systematically with needle orientation. In case of needle biopsy procedures, the biopsy target is located in the middle of the needle biopsy gap (at around 10 mm from the needle tip for the needle we used). As shown in Fig. 9 left, the gap into the needle inner stylet creates a shift in artifact comparatively with the other segments, altering the targeting error. For example, Table 4 shows the transverse plane needle artifact position error mean and standard deviation averaged for the case presented in Fig. 5 considering the whole needle (top part) versus considering only the needle biopsy gap segment (bottom part). The average error in the X direction is slightly higher for the biopsy gap segment (0.53 mm) that for the whole needle (0.48 mm) with similar standard deviation (0.16 and 0.17 respectively). In Y direction, the average error for biopsy gap segment (0.41 mm) is almost half of the error for the whole needle (0.74 mm) with close standard deviations. The smaller “shift” of the error in Y direction along the biopsy gap segment is related to lack of material in that area and needle axial orientation.

The needle tip artifact was seen to bend toward the B_0 direction, corroborating other studies [34, 35]: the needle tip artifact is beyond the needle tip and is “bent” toward the B_0 direction. For our study, it was important to understand how to eliminate the influence of this artifact. Our assumption was that the glass and titanium needles have the same depth. In our study, we considered just the slices containing the glass needle voids and the correspondent slices for titanium needle artifact. For a clinical biopsy procedure, the needle tip artifact is practically not relevant because the target is at around 10 mm from the needle tip.

The distance between the surface coil and the endorectal coil has no effect on the location of the artifact. The effect of the coil distance on the void artifact would be of consideration only (1) if the coils are placed too close together, which could create “coupling”. The coupling would affect the whole image and not just the artifact, or (2) if the coils are placed too far away and as such very low signal can be received from the volume where the needle is located. Both situations would affect at least the large-local region not just the void artifact. In practice, the former situation, coils too close together, was and is always controlled in clinical cases as it can be a patient safety issue, and usually the anatomy itself provides sufficient separation. It is also controlled in all phantom experiments as well by using plastic or similar stands to rest the prostate phantom on above the surface coil.

The phantom and associated setup was designed to approximate conditions occurring in actual MR needle confirmation imaging of typical adult male subjects. The orientations of the needle studied herein were selected to include the entire range of the needle angles required to provide full transrectal needle biopsy access of the prostate, accommodating the normal variation of prostate size and position occurring in adult males.

The localization of the titanium biopsy needle artifact provides a consistent offset value between the true needle position and the needle void position on confirmation images. To improve the accuracy of the biopsy, it will be necessary to visualize artifact-corrected true needle positions on confirmation images as an automatic process. Such artifact correction and visualization process should be examined for safety and quality assurance of the intervention.

VI. Conclusion

This study addresses the effect of needle artifact displacement for the scan sequences, and for the specific range of needle orientations (orientations with respect to B_0, frequency encoding direction, gradient encoding direction) arising in our clinical 3.0 T MRI-guided transrectal needle biopsy procedures of the prostate. We conclude the following:

1. The titanium needle-void artifacts in T2 confirmation imagery form a straight line parallel to the actual needle position in slices in which the needle is physically present.
2. The needle tip artifact can extend 9 mm beyond the actual needle tip location shown in Fig. 10, and it exhibits strong curvature in the direction of the B_0 magnetic field.
3. The magnitude of the titanium needle void displacement increases monotonically with the needle’s angle with respect to the scanner’s B_0 magnetic field direction.
4. The needle void displacement is systematic in the Y (anterior) frequency encoding direction, and with large variance. This corroborates previous reports [40, 41].
5. The needle void displacement is smaller in the X (right) phase encoding direction, with small variance.
6. All of the observed titanium needle void artifact displacements are less than 2 mm from the actual needle location, smaller than the radius of the significant tumor size of 2 ~ 5 mm reported in clinical studies [45, 46].

These results are likely to be relevant to any 3T transrectal MRI-guided system that employs similar confirmation scans to confirm the location of titanium needle biopsies.

Acknowledgments

We are grateful to Dr. Andras Lasso (Queen's University, Canada) for his support on 3D Slicer and image processing.

This study was supported by the National Institutes of Health (NIH) under Grant RO1-EB02963. Gabor Fichtinger was funded as Cancer Care Ontario Research Chair.

References

1. Song S, Cho N, Iordachita I, Guion P, Fichtinger G, Whitcomb L. A Study of Needle Image Artifact Localization in onfirmation Imaging of MRI-guided Robotic Prostate Biopsy. IEEE Int Robotics and Automation (ICRA). May 9.2011 :4834–4839.
2. Chowning SL, Susil RC, Krieger A, Fichtinger G, Whitcomb LL, Atalar E. A preliminary analysis and model of prostate injection distributions. Prostate. 2006; 66(4):344–57. [PubMed: 16302267]
3. Susil RC, Krieger A, Derbyshire JA, Tanacs A, Whitcomb LL, Fichtinger G, Atalar E. System for MR Image-guided Prostate Interventions: Canine Study. Radiology. Sep; 2003 228(3):886–894. [PubMed: 12954903]
4. Krieger A, Susil RC, Ménard C, Coleman JA, Fichtinger G, Atalar E, Whitcomb LL. Design of a novel MRI compatible manipulator for image guided prostate interventions. IEEE Transactions on Biomedical Engineering. Feb; 2005 52(2):306–313. [PubMed: 15709668]
5. Krieger A, Iordachita I, Guion P, Singh A, Kaushal A, Pinto P, Champhausen K, Fichtinger G, Whitcomb L. An MRI-Compatible Robotic System with Hybrid Tracking for MRI-guided Prostate Intervention. IEEE Transactions on Biomedical Engineering. Nov; 2011 58(11):3049–3060. [PubMed: 22009867]
6. Krieger, A. PhD. Department of Mechanical Engineering, Johns Hopkins University; Baltimore: 2008. Advances in MRI Guided Robotic Intervention.
7. Krieger A, Song SE, Bongjoon Cho N, Iordachita II, Guion P, Fichtinger G, Whitcomb LL. Development and Evaluation of an Actuated MRI-Compatible Robotic System for MRI-Guided Prostate Intervention. Mechatronics, IEEE/ASME Transactions on. 2011; 99:1–12.
8. American_Cancer_Society. Cancer Facts & Figures 2012. 2012. http://www.cancer.org/Research/CancerFactsFigures/CancerFactsFigures/ACSPC-031941
9. Presti JC. Prostate cancer: assessment of risk using digital rectal examination, tumor grade, prostate-specific antigen, and systematic biopsy. Radiologic Clinics of North America. Jan; 2000 38(1):49–58. [PubMed: 10664666]
10. Norberg M, Egevad L, Holmberg L, SparŽn P, NorlŽn BJ, Busch C. The sextant protocol for ultrasound-guided core biopsies of the prostate underestimates the presence of cancer. Urology. Oct; 1997 50(4):562–566. [PubMed: 9338732]
11. Rabbani F, Stroumbakis N, Kava BR, Cookson MS, Fair WR. Incidence and clinical significance of false-negative sextant prostate biopsies. Journal of Urology. Apr; 1998 159(4):1247–1250. [PubMed: 9507846]
12. Taira AV, Merrick GS, Galbreath RW, Andreini H, Taubenslag W, Curtis R, Butler WM, Adamovich E, Wallner KE. Performance of transperineal template-guided mapping biopsy in detecting prostate cancer in the initial and repeat biopsy setting. Prostate Cancer Prostatic Dis. Sep 29.2009
13. Wefer AE, Hricak H, Vigneron DB, Coakley FV, Lu Y, Wefer J, Mueller-Lisse U, Carroll PR, Kurhanewicz J. Sextant localization of prostate cancer: comparison of sextant biopsy, magnetic resonance imaging and magnetic resonance spectroscopic imaging with step section histology. Journal of Urology. Aug; 2000 164(2):400–404. [PubMed: 10893595]
14. Terris MK. Strategies for repeat prostate biopsies. Curr Urol Rep. May; 2009 10(3):172–8. [PubMed: 19371473]
15. Pondman KM, Futterer JJ, ten Haken B, Schultze Kool LJ, Witjes JA, Hambrock T, Macura KJ, Barentsz JO. MR-guided biopsy of the prostate: an overview of techniques and a systematic review. Eur Urol. Sep; 2008 54(3):517–27. [PubMed: 18571309]

16. Fei, B.; Lee, Z.; Boll, D.; Duerk, J.; Lewin, J.; Wilson, D. Image registration and fusion for interventional MRI-guided thermal ablation of the prostate cancer. The Sixth Annual International Conference on Medical Imaging Computing & Computer Assisted Intervention (MICCAI). Lecture Notes in Computer Science (LNCS); 2003. p. 364-372.
17. Beyersdorff D, Winkel A, Hamm B, Lenk S, Loening SA, Taupitz M. MR imaging-guided prostate biopsy with a closed MR unit at 1.5 T: initial results. Radiology. Feb; 2005 234(2):576–81. [PubMed: 15616117]
18. Engelhard K, Hollenbach HP, Kiefer B, Winkel A, Goeb K, Engehausen D. Prostate biopsy in the supine position in a standard 1.5-T scanner under real time MR-imaging control using a MR-compatible endorectal biopsy device. European Radiology. Jun; 2006 16(6):1237–1243. [PubMed: 16447048]
19. Schouten MG, Ansems J, Renema WK, Bosboom D, Scheenen TW, Futterer JJ. The accuracy and safety aspects of a novel robotic needle guide manipulator to perform transrectal prostate biopsies. Med Phys. Sep; 2010 37(9):4744–50. [PubMed: 20964192]
20. Elhawary H, Zivanovic A, Rea M, Davies B, Besant C, McRobbie D, de Souza N, Young I, Lampérth M. The Feasibility of MR-Image Guided Prostate Biopsy Using Piezoceramic Motors Inside or Near to the Magnet Isocentre. Medical Image Computing and Computer-Assisted Intervention – MICCAI 2006. 2006; 9:519–526.
21. Yakar D, Schouten MG, Bosboom DG, Barentsz JO, Scheenen TW, Futterer JJ. Feasibility of a pneumatically actuated MR-compatible robot for transrectal prostate biopsy guidance. Radiology. Jul; 2011 260(1):241–7. [PubMed: 21406625]
22. D'Amico AV, Tempany CM, Cormack R, Hata N, Jinzaki M, Tuncali K, Weinstein M, Richie JP. Transperineal magnetic resonance image guided prostate biopsy. J Urol. Aug; 2000 164(2):385–7. [PubMed: 10893591]
23. Chinzei K, Hata N, Jolesz F, Kikinis R. MR Compatible Surgical Assist Robot: System Integration and Preliminary Feasibility Study. Medical Image Computing and Computer-Assisted Intervention – MICCAI 2000. 2000; 3:921–930.
24. DiMaio SP, Kacher DF, Ellis RE, Fichtinger G, Hata N, Zientara GP, Panych LP, Kikinis R, Jolesz FA. Needle artifact localization in 3T MR images. Studies in Health Technology and Informatics. 2006; 119:120–125. [PubMed: 16404029]
25. Tadakuma K, Devita LM, Plante J-s, Shaoze Y, Dubowsky S. The experimental study of a precision parallel manipulator with binary actuation: With application to MRI cancer treatment. IEEE Int Robotics and Automation (ICRA). May 19–23.2008 :2503–2508.
26. Stoianovici D, Song D, Petrisor D, Ursu D, Mazilu D, Muntener M, Schar M, Patriciu A. MRI Stealth" robot for prostate interventions. Minim Invasive Ther Allied Technol. 2007; 16(4):241–8. [PubMed: 17763098]
27. Fischer GS, Iordachita I, Csoma C, Tokuda J, DiMaio SP, Tempany CM, Hata N, Fichtinger G. MRI-Compatible Pneumatic Robot for Transperineal Prostate Needle Placement. IEEE/ASME Transactions on Mechatronics. Jun; 2008 13(3):295–305. [PubMed: 21057608]
28. Song S, Cho NB, Fischer G, Hata N, Tempany C, Fichtinger G, Iordachita I. Development of a pneumatic robot for mri-guided transperineal prostate biopsy and brachytherapy: New approaches. IEEE Int Robotics and Automation (ICRA). 2010:2580–2585.
29. Song, S.; Cho, N.; Tokuda, J.; Hata, N.; Tempany, C.; Fichtinger, G.; Iordachita, I. Preliminary Evaluation of a MRI-compatible Modular Robotic System for MRI-guided Prostate Interventions. Proc IEEE RAS EMBS Int Conf Biomed Robot Biomechatron; Sep 26, 2010; p. 796-801.
30. Goldenberg AA, Trachtenberg J, Kucharczyk W, Haider YY, Ma LM, Weersink R, Raoufi C. Robotic System for Closed-Bore MRI-Guided Prostatic Interventions. IEEE/ASME Transactions on Mechatronics. Jun 13; 2008 13(3):374–379.
31. van den Bosch MR, Moman MR, van Vulpen M, Battermann JJ, Duiveman E, van Schelven LJ, de Leeuw H, Lagendijk JJ, Moerland MA. MRI-guided robotic system for transperineal prostate interventions: proof of principle. Phys Med Biol. Mar 7; 2010 55(5):N133–40. [PubMed: 20145293]

32. Su, H.; Zervas, M.; Cole, G.; Furlong, C.; Fischer, G. Real-time MRI-Guided Needle Placement Robot with Integrated Fiber Optic Force Sensing. IEEE Int Conf Robot Autom; Sep 9, 2011; p. 1583-1588.
33. Zangos S, Eichler K, Engelmann K, Ahmed M, Dettmer S, Herzog C, Pegios W, Wetter A, Lehnert T, Mack MG, Vogl TJ. MR-guided transgluteal biopsies with an open low-field system in patients with clinically suspected prostate cancer: technique and preliminary results. Eur Radiol. Jan; 2005 15(1):174–82. [PubMed: 15351902]
34. Zangos S, Herzog C, Eichler K, Hammerstingl R, Lukoschek A, Guthmann S, Gutmann B, Schoepf UJ, Costello P, Vogl TJ. MR-compatible assistance system for punction in a high-field system: device and feasibility of transgluteal biopsies of the prostate gland. Eur Radiol. Apr; 2007 17(4):1118–24. [PubMed: 17031454]
35. Schell B, Eichler K, Mack MG, Muller C, Kerl JM, Czerny C, Beeres M, Thalhammer A, Vogl TJ, Zangos S. Rofo. Oct 27.2011
36. Zangos S, Melzer A, Eichler K, Sadighi C, Thalhammer A, Bodelle B, Wolf R, Gruber-Rouh T, Proschek D, Hammerstingl R, Muller C, Mack MG, Vogl TJ. MR-compatible assistance system for biopsy in a high-field-strength system: initial results in patients with suspicious prostate lesions. Radiology. Jun; 2011 259(3):903–10. [PubMed: 21364080]
37. Blumenfeld P, Hata N, DiMaio S, Zou K, Haker S, Fichtinger G, Tempany CMC. Transperineal prostate biopsy under magnetic resonance image guidance: a needle placement accuracy study. Journal of Magnetic Resonance Imaging. Sep; 2007 26(3):688–694. [PubMed: 17729363]
38. Lufkin R, Teresi L, Chiu L, Hanafee W. A technique for MR-guided needle placement. Am J Roentgenol. 1998; 151(1):193–196. [PubMed: 3259804]
39. Lewin J, Duerk J, Jain V, Petersilge C, Chao C, Haaga J. Needle localization in MR-guided biopsy and aspiration: effects of field strength, sequence design, and magnetic field orientation. American Journal of Roentgenology. 1996; 166:1337–1345. [PubMed: 8633445]
40. Wachowicz K, Thomas SD, Fallone BG. Characterization of the susceptibility artifact around a prostate brachytherapy seed in MRI. Med Phys. Dec; 2006 33(12):4459–67. [PubMed: 17278797]
41. Lagerburg V, Moerland MA, Seppenwoolde JH, Lagendijk JJW. Simulation of the artefact of an iodine seed placed at the needle tip in MRI-guided prostate brachytherapy. Phys Med Biol. 2008; 53:59.
42. Thomas SD, Wachowicz K, Fallone BG. MRI of prostate brachytherapy seeds at high field: A study in phantom. Medical Physics. 2009; 36(11):5228–5234. [PubMed: 19994533]
43. F. D. A. U.S. Department of Health and Human Services, Center for Devices and Radiological Health. Criteria for signicant risk investigations of magnetic resonance diagnostic devices. 2003.
44. Metzger, G.; Krieger, A.; Guion, P.; Ferhanoglu, O.; Choyke, P.; Menard, C.; Atalar, E. Predicting true SAR limits for in vivo imaging in MR guided prostate procedures. 5th Interventional MRI Symposium; 2004.
45. Haider MA, van der Kwast TH, Tanguay J, Evans AJ, Hashmi AT, Lockwood G, Trachtenberg J. Combined T2-weighted and diffusion-weighted MRI for localization of prostate cancer. AJR Am J Roentgenol. Aug; 2007 189(2):323–8. [PubMed: 17646457]
46. Nakashima J, Tanimoto A, Imai Y, Mukai M, Horiguchi Y, Nakagawa K, Oya M, Ohigashi T, Marumo K, Murai M. Endorectal MRI for prediction of tumor site, tumor size, and local extension of prostate cancer. Urology. Jul; 2004 64(1):101–105. [PubMed: 15245944]

Biographies

Sang-Eun Song (M'10) received the M.Sc. degree in mechanical systems engineering from the University of Liverpool, Liverpool, U.K., in 2000, and the Ph.D. degree in mechanical engineering (medical robotics) from Imperial College London, London, U.K., in 2005.

He was a Research Scientist at the Laboratory for Computational Sensing and Robotics, The Johns Hopkins University, Baltimore, MD. He is currently a Research Associate in the Radiology Department, Brigham & Women's Hospital and Harvard Medical School, Boston, MA. His research interests include design, control, and clinical implementation of surgical robotic systems.

Nathan Bongjoon Cho received the M.S. degree in computer science from The Johns Hopkins University, Baltimore, MD, in 2008.

He is currently a Research Engineer in the Laboratory for Computational Sensing and Robotics, The Johns Hopkins University. His research interests include medical robotics and image-guided interventions with MRI and CT.

Iulian I. Iordachita (M'08) received the B.Eng. degree in mechanical engineering, the M.Eng. degree in industrial robots, and the Ph.D. degree in mechanical engineering in 1984, 1989, and 1996, respectively, all from the University of Craiova, Craiova, Romania.

He is currently an Assistant Research Professor in the Department of Mechanical Engineering and the Laboratory for Computational Sensing and Robotics, The Johns Hopkins University, Baltimore, MD, where he is involved in research on robotics, in particular, robotic hardware. His current research interests include design and manufacturing

of surgical instrumentation and devices, medical robots, and mechanisms and mechanical transmissions for robots.

Peter Guion (M'05) received B.S. degrees in mechanical and electrical engineering from Virginia Polytechnic Institute and State University, Blacksburg, in 1996, and the University of Maryland, College Park, in 1999, respectively, and the M.S. degree in aerospace engineering from the University of Maryland, College Park, in 2003.

He is currently the Staff Engineer at the Radiation Oncology Branch, National Cancer Institute, Bethesda, MD. His research interests include robotics and control systems, with a focus on MRI-guided procedures.

Gabor Fichtinger (M'04) received the Ph.D. degree in computer science from the Technical University of Budapest, Budapest, Hungary, in 1990.

He is currently a Professor in the School of Computing, with cross appointments in the Departments of Mechanical and Material Engineering, Electrical and Computer Engineering, and Surgery, Queen's University, Kingston, ON, Canada, where he directs the Percutaneous Surgery Laboratory. His research specializes on system development for computer assisted interventions, with special focus on image-guided oncology applications.

Dr. Fichtinger holds a Level-1 Cancer Care Ontario Research Chair in Cancer Imaging.

Aradhana Kaushal received the B.A./M.D. degree (magna cum laude) from Boston University, Boston, MA, in 2002. She completed her internship in internal medicine at Lenox Hill Hospital, a teaching hospital of New York University, and a residency in radiation oncology at Thomas Jefferson University Hospital, where she was a chief resident during her last year of residency.

For a year, she was with the National Cancer Institute, Bethesda, MD, where she was engaged in research on mechanisms for resistance of tumor cells to oxidative stress under the supervision of Dr. N. Coleman and Dr. D. Gius. Her current clinical research interests include prostate and pediatric malignancies. She is Clinical Director and Staff Clinician, Radiation Oncology Branch, National Cancer Institute, National Institutes of Health, Bethesda, MD.

Dr. Kaushal is board certified by the American Board of Radiology.

Kevin Camphausen received the B.S. degree in biology from Purdue University, West Lafayette, IN, in 1988. He completed his M.D. degree and medical internship at Georgetown University Medical Center, Washington, DC, in 1996 and 1997, respectively. He then completed his residency in radiation oncology at the Joint Center of Radiation Therapy at Harvard Medical School, in 2001, where he was engaged in research on the interactions of antiangiogenic therapy and radiotherapy in the laboratory of Dr. J. Folkman.

In 2001, he joined the Radiation Oncology Branch as a tenure track investigator. In 2007, he joined the National Institutes of Health, where he was promoted to be the Chief of the Radiation Oncology Branch, Center for Cancer Research, National Cancer Institute in 2007. He is a Physician/Scientist, who has a laboratory program that focuses on the development and characterization of agents that alter the tumoral response to radiation. He has been successful in translating his work from the laboratory to the clinic. He is an internationally recognized leader in his field and an expert in the field of drug-induced tumor radiosensitization including the use of anti-angiogenic agents in combination with radiotherapy.

Louis L. Whitcomb (S’86–M’95–SM’02–F’11) received the Ph.D. degree in electrical engineering from Yale University, New Haven, CT, 1992.

He is currently a Professor in the Department of Mechanical Engineering, with secondary appointment in the Department of Computer Science, Johns Hopkins University, Baltimore, MD, where he directs the Laboratory for Computational Sensing and Robotics. His research interests include the design, dynamics, and control of robotic systems, with focus on image-guided systems for intervention in extreme environments, with focus on MRI-guided international systems.

Dr. Whitcomb is the Louis R. Sardella Faculty Scholar at the G.W. C.Whiting School of Engineering, The Johns Hopkins University.

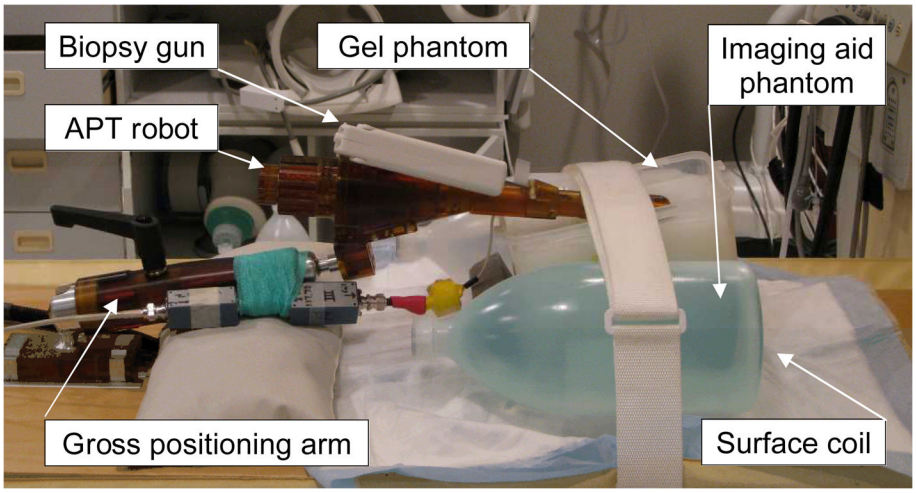

Fig. 1.
Photograph of the needle artifact study experimental setup, showing the APT transrectal prostate interventional robot with a 14G biopsy gun inserted into custom made gel phantom in a 3T Philips Achieva MRI scanner.

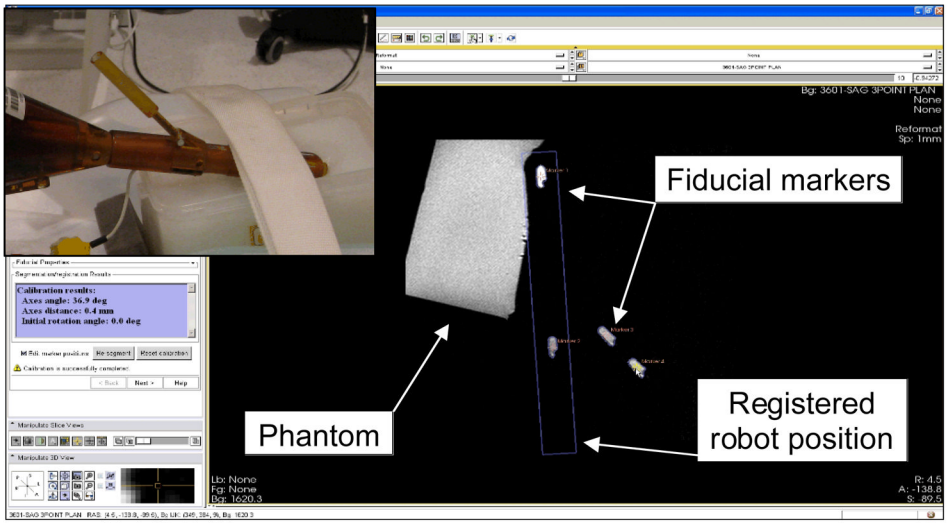

Fig. 2.

A screenshot of APT robot registration in the 3D Slicer ProstateNav module. In the marker plane sagittal view, four embedded fiducial markers are identified to locate the robot position in scanner space. The inset shows the APT with the detachable marker tube containing two markers in line.

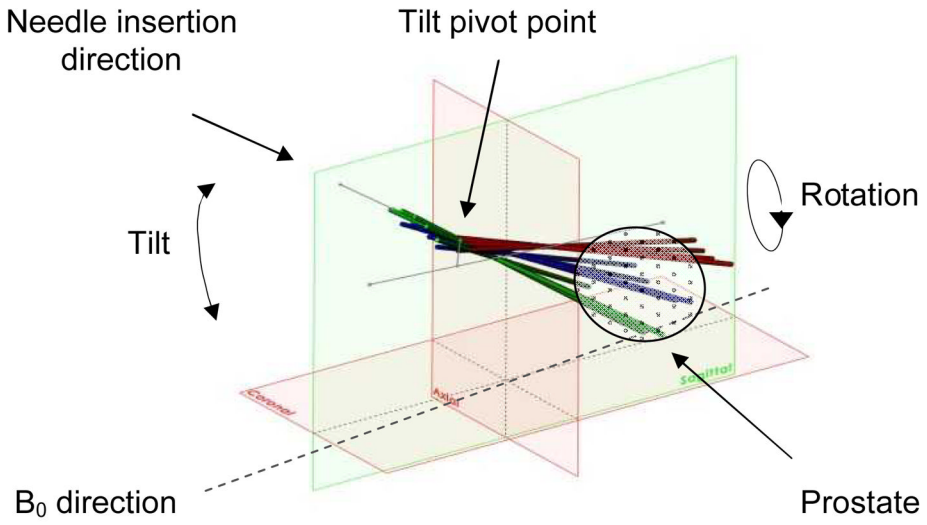

Fig. 3.

Model of various needle insertion angles: tilt angle of 18°, 28°, 38° and rotation angle of −30°, −15°, 0°, 15°, 30°. Reference lines represent the initial needle insertion axis, the tilt axis and the line between rotation axis and the pivot point of tilt angle.

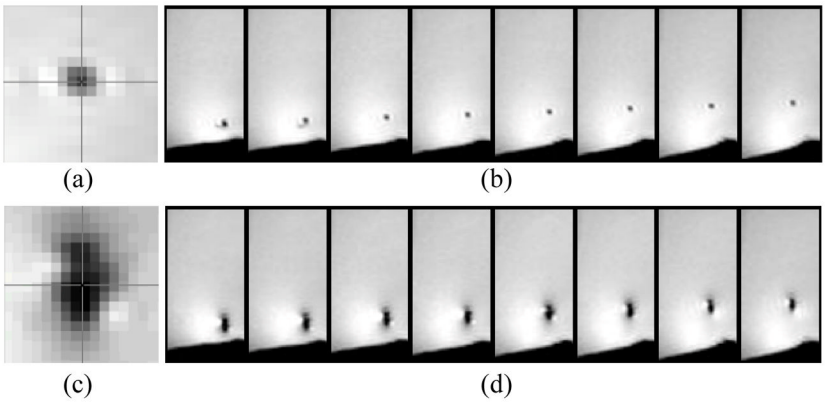

Fig. 4.

Representative images of glass rod and titanium needle artifacts: (a) zoomed view of typical glass rod artifact, (b) glass rod artifact images from inferior to superior direction (left to right), (c) and (d) are of titanium needle.

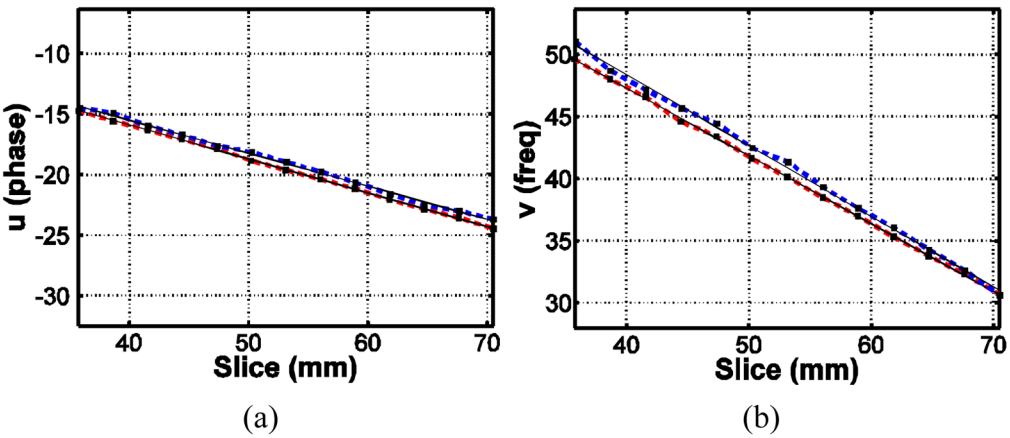

(a) (b)

Fig. 5.

MRI needle void locations for titanium needle (blue, upper line) and glass rod (red, lower line) and corresponding least-square best-fit lines (solid black lines). The left plot shows coronal view with phase-encoding direction along the Y-axis, and the B_0-field along the X-axis. The right plot shows sagittal view with frequency encoding direction along the Y-axis and the B_0-field along the X-axis.

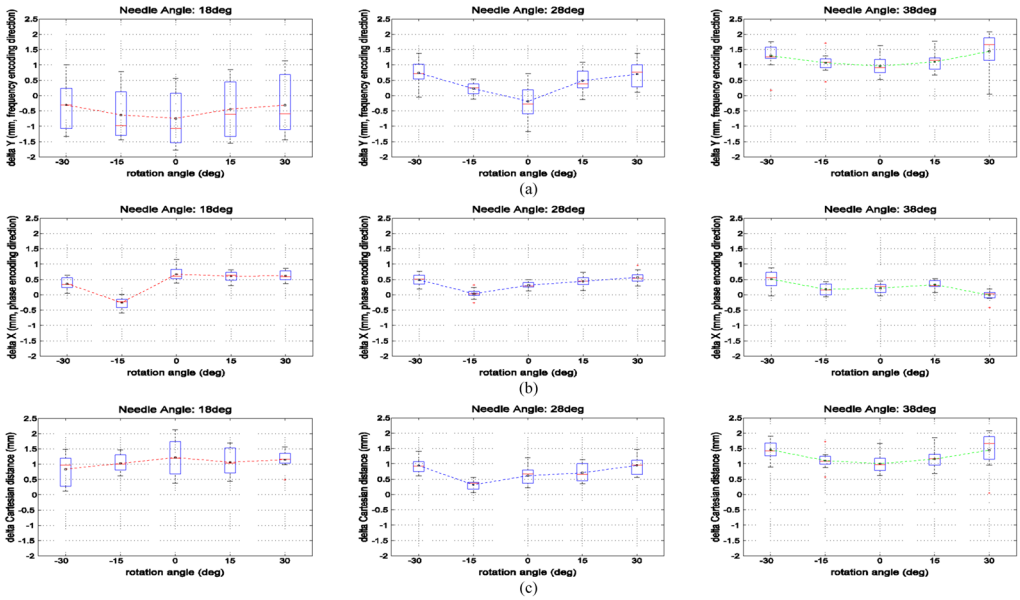

Fig. 6.

(a) shows boxplots of the titanium needle void displacement in the Y (anterior) frequency encoding direction for each of the 15 combinations of needle tilt angles and rotation angles. Fig. 6 (b) shows boxplots of the titanium needle void displacement in the X (right) phase encoding direction for each of the 15 combinations of needle tilt angles and rotation angles. Fig. 6 (c) shows boxplots of the titanium needle void total displacement distance for each of the 15 combinations of needle tilt angles and rotation angles. The total displacement distance for tilt angle of 18°, 28° and 38° over all rotation angles was, respectively, +1.06 mm, +0.70 mm, and +1.23 mm.

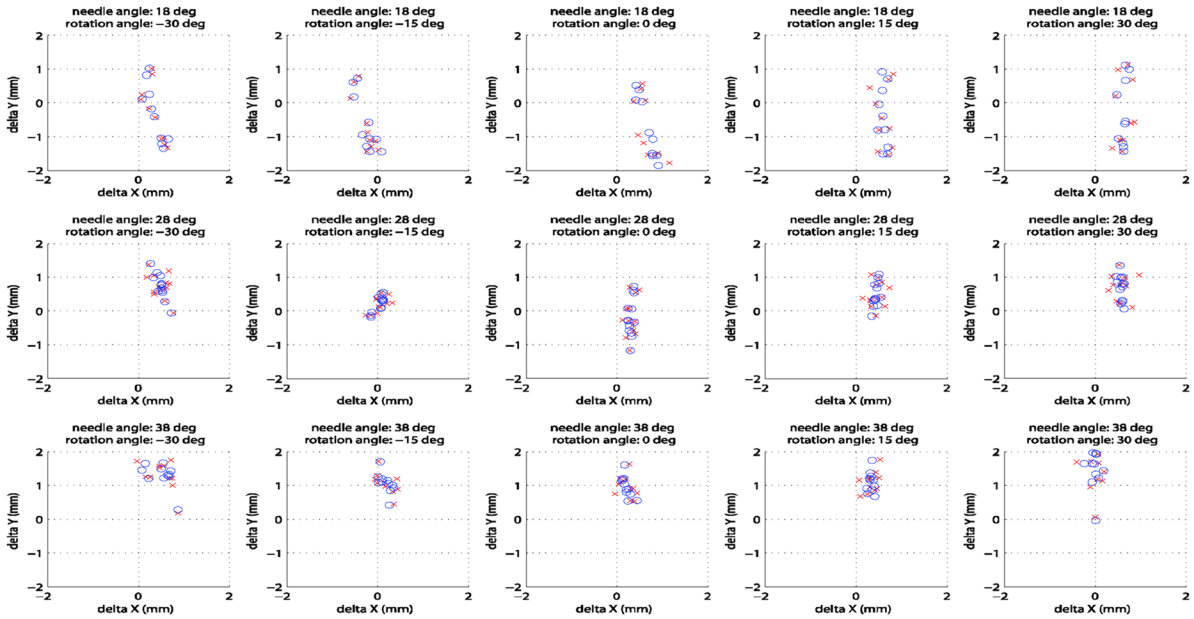

Fig. 7.

Axial-plane needle artifact position error for the 15 tested needle orientations. The plots show the axial plane difference between the center of the titanium needle void and the center of the glass needle void for all axial image slices physically intersecting the needles. The needle locations are physically identical, but the titanium needle image void is displaced with respect to the actual needle position that is given by the glass rod. The rows represent needle tilt angles of (from top to bottom) +18°, +28°, and +38°. The columns represent needle rotation angles of −30°, −15°, 0°, +15°, and +30°. ‘delta X’ and ‘delta Y’ represent R (right) and A (anterior) coordinate directions in scanner coordinates, respectively. ‘○’ represents the error value from manually located artifact center position, and ‘×’ represents that from fitted line as seen in Fig. 5.

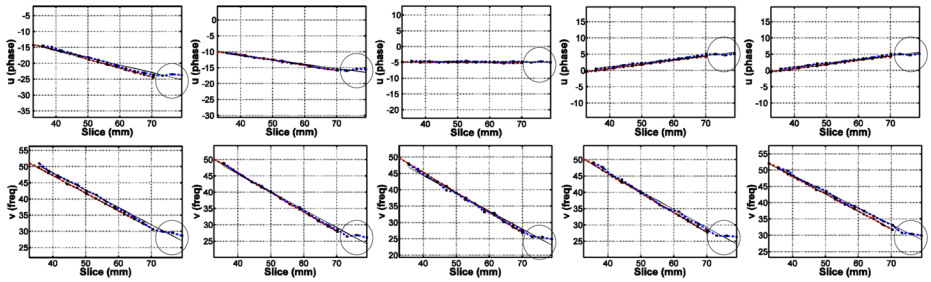

Fig. 8.

Representative plots of glass rod and titanium needle artifact center positions and fitted line at various insertion angles including entire recognizable titanium needle artifact, showing "bending" of the titanium needle tip artifact towards B_0 direction (in circle). First row: coronal plane plots of −30°, −15°, 0°, 15°, 30° rotation angles (from left) with 28° tilt angle, second row: corresponding sagittal plane plots.

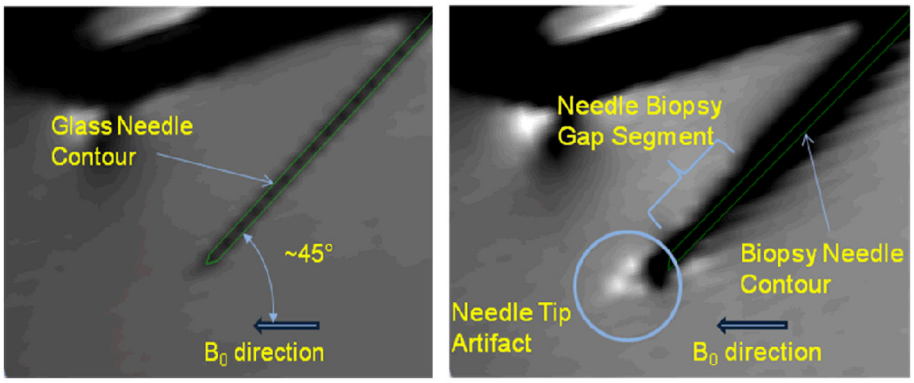

Fig. 9.
Artifacts in sagittal view for glass rod (left) and titanium needle (right) with needle tilt angle 28° and rotation angle 0°.

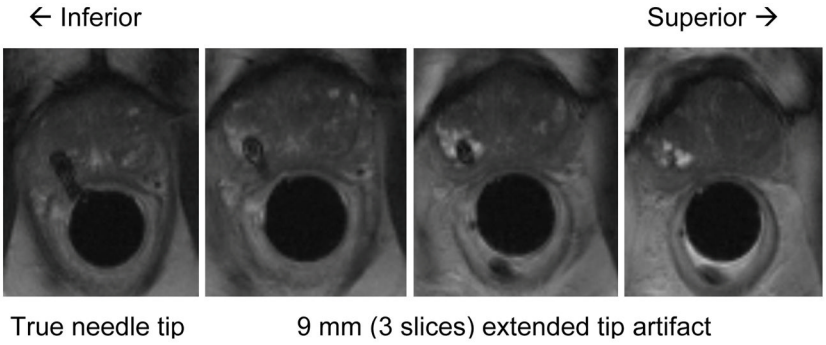

Fig. 10.

An example of biopsy needle position confirmation image during prostate biopsy procedure using the APT robot. Although needle void is found in all images, the artifact study suggests that the true needle tip position is located at the first image plane and needle void in the last three (from right) are only extended artifact. Hence, clinician can confirm whether the needle is placed at designated target by checking the fourth needle void image from the last (in case of 3 mm image slice thickness).

TABLE 1

MRI scan parameters for needle artifact study

Slice thickness (mm)	3
Number of pixel	256 × 256
Pixel size (mm)	0.859375
Field of view (mm)	220 × 256
Number of slices	28
TE (echo time) (ms)	70
TR (repetition time) (ms)	11416
Flip angle (°)	90
NEX (number of excitations)	1
Pixel bandwidth (Hz/pixel)	1554

TABLE 2

RMS residuals (mm) for the least-square line fits for each of the 15 insertion positions for the glass rod (top) and titanium needle (bottom)

Glass rod RMS line fit residuals (mm)					
	Rotation angle (deg)				
Needle angle (deg)	**−30**	**−15**	**0**	**15**	**30**
18	0.04	0.05	0.09	0.09	0.10
28	0.06	0.07	0.08	0.06	0.07
38	0.12	0.07	0.09	0.05	0.09

Titanium needle RMS line fit residuals (mm)					
	Rotation angle (deg)				
Needle angle (deg)	−30	−15	0	15	30
18	0.11	0.06	0.09	0.15	0.12
28	0.12	0.09	0.09	0.10	0.15
38	0.17	0.09	0.09	0.14	0.14

TABLE 3

Transverse plane needle artifact position error mean and standard deviation averaged over the 15 tested needle orientations. ‘delta X and ‘delta Y’ represent R (right) and A (anterior) coordinate directions in scanner coordinates, respectively

	delta X (mm)	delta X std (mm)	delta Y (mm)	delta Y std (mm)
Titanium – Glass (manual)	0.32	0.19	0.38	0.57
Titanium – Glass (fitted line)	0.32	0.13	0.38	0.56

TABLE 4

Axial-plane needle artifact position error mean and standard deviation for the case presented in Fig. 5. averaged over the whole needle length (top part) and over the needle biopsy gap segment (bottom part).

	delta X (mm)	delta X std (mm)	delta Y (mm)	delta Y std (mm)
Titanium – Glass (manual)	0.48	0.17	0.74	0.38
Titanium – Glass (fitted line)	0.48	0.11	0.74	0.37
Titanium – Glass (manual)	0.53	0.16	0.41	0.30
Titanium – Glass (fitted line)	0.53	0.16	0.41	0.30